Water Air Soil Pollut (2023) 234:420
https://doi.org/10.1007/s11270-023-06417-2

Removal of Methyl Orange in Aqueous Solutions Using Hydrochloric Acid-Modified Kaolinite Supported Nanosized Zero-Valent Iron

Yunfeng Tan · Yangyang Zhang · Bo Zu · Yunxia Zhang · Chunli Zheng · Kejun Chen

Received: 29 November 2022 / Accepted: 6 June 2023 / Published online: 26 June 2023

Abstract This study presents an efficient application of the Fenton reaction for the degradation of methyl orange (MO), utilizing a composite of hydrochloric acid-modified kaolinite supported nanosized zero-valent iron (mk-nZVI). The successful loading of Fe^0 onto the hydrochloric acid–modified kaolinite was confirmed through scanning electron microscopy, X-ray diffraction, and Fourier transform infrared spectroscopy analyses. Key variables, such as solution pH, reaction temperature, mk-nZVI dose, initial MO solution concentration, and H_2O_2 concentration, were manipulated to examine the efficacy of the mk-nZVI/H_2O_2 system in the degradation of MO. The system demonstrated improved degradation performance with decreased pH and increased temperature. Under the following conditions: an initial pH of 5.6, a reaction temperature of 25 °C, an mk-nZVI dose of 2 g/L, an initial MO solution concentration of 100 mg/L, and an H_2O_2 concentration of 74.8 mmol/L, an MO degradation of 96.56% was achieved using the mk-nZVI/H_2O_2-based Fenton-like reaction. This performance was markedly superior to the traditional Fenton method in decolorizing MO solutions. UV–Vis spectroscopy demonstrated the mk-nZVI/H_2O_2-based Fenton-like reaction's effectiveness in degrading MO's azo structure. The degradation of MO was primarily attributed to the action of surface-bounded hydroxyl radicals. The findings indicate that the synthesized mk-nZVI composite holds promise for efficient treatment of MO in water, establishing it as a prospective composite material for wastewater remediation.

Y. Tan · Y. Zhang (✉) · B. Zu (✉) · Y. Zhang
College of River and Ocean Engineering, Chongqing Jiaotong University, Chongqing 400074, China
e-mail: yyz@cqjtu.edu.cn

B. Zu
e-mail: zubo@cqjtu.edu.cn

Y. Tan
e-mail: 1677819280@qq.com

Y. Zhang
e-mail: 429896842@qq.com

Y. Zhang
Chongqing Bureau of Geology and Mineral Resources, Chongqing 401121, China

Y. Zhang
Chongqing Gangli Environmental Protection Co., LTD, Chongqing 400042, China

C. Zheng
Department of Environmental Science and Engineering, Xi'an Jiaotong University, Xi'an 710049, China
e-mail: clzhen@mail.xjtu.edu.cn

K. Chen
China Merchants Ecological Environmental Protection Technology Co., LTD., Chongqing 400067, China
e-mail: chenkejun@cmhk.com

Keywords Kaolinite · Nanosized zero-valent iron · Methyl orange · Fenton

1 Introduction

In the context of burgeoning industrial advancements, the widespread application of organic dyes encompassing azo groups has become integral to various manufacturing processes, driven by the incessant momentum of global industrialization. However, this progress brings with it a pressing challenge related to the management of industrial wastewater. Among the myriad contributors to this issue, the textile industry stands as the most substantial, accounting for 54% of the worldwide dye wastewater. Additional significant contributors include the printing and dyeing, paper and pulp, leather and paint, as well as dye manufacturing industries, which are responsible for 21%, 10%, 8%, and 7% of the total dye wastewater, respectively (De Gisi et al., 2016). Azo dyes, which are the main source of dye wastewater pollution, are extremely difficult to degrade because of their complex structures and the generation of several metabolic intermediates (Varjani et al., 2020). In addition, a few azo dyes may produce carcinogenic aromatic amines in chemical reaction decomposition. Long-term exposure to these compounds will pose different degrees of risk to human health. Due to the large amount of azo dye wastewater discharge and high concentration of pollutants, it poses a serious threat to the environment and residents' health, making it one of the important problems of water pollution. In recent years, scholars have conducted a large number of experimental treatments on dye wastewater, using methods from fields such as physics (Waheed et al., 2021), chemistry (Refat et al., 2021; Zheng et al., 2020), and biology (Kapoor et al., 2021; Wang et al., 2020). However, the efficient treatment of dye industrial wastewater is still a hot issue to be solved urgently and has great challenges. Therefore, the development of composite materials that can efficiently remove dye from wastewater is of great importance.

Nanosized zero-valent iron (nZVI) is a type of nanoparticle material that presents certain unique properties. These properties, known as surface effects, emerge due to an abrupt increase in the ratio of surface atoms to total atoms as particle size decreases (Galdames et al., 2020; Li et al., 2021). nZVI is frequently used for in situ and ectopic remediation of groundwater and soil pollution owing to its large specific surface area, high reactivity, free migration in water, and environmental friendliness (Marcon et al., 2021). However, the shortcomings of nZVI, such as easy oxidation by non-target chemicals and particle aggregation, reduce the reaction efficiency of nZVI and limit the direct application of nZVI in the remediation of azo dye wastewater, which usually leads to a rapid decline in catalytic activity, material waste, and can even limit its economic feasibility.

To address the aforementioned shortcomings of nZVI, various strategies have been employed. These include the use of iron-based catalytic substances, loaded or doped with metal active components. These substances are applied to the Fenton oxidation method, with the goals of reducing the rapid oxidation of nZVI itself, preventing particle agglomeration, and ultimately improving the activity and recovery effect of the catalyst. nZVI is currently used to degrade azo dyes, such as methyl orange (Shi et al., 2020), Congo red (Tanwar et al., 2017), orange-yellow series of dyes (I–IV) (Bastidas et al., 2018; Park et al., 2019), in wastewater. Moreover, Fenton-like reaction can assist in the treatment of various organic pollutants, such as azo dyes (Tang et al., 2020), inorganic acids (Arts et al., 2021), and phenolic compounds (Xie et al., 2019). The decolorization mechanism of azo dye wastewater with nZVI primarily involves a coexistence system containing Fe^0, Fe^{2+} and Fe^{3+}. In this system, the ·OH free radical preferentially breaks the azo group (-N=N-), leading to the decolorization of the dye (Yu et al., 2014).

In this study, our focus was on the degradation processes of methyl orange. Kaolinite, an economical and readily available material, has been shown to act as an effective adsorbent for various pollutants (Gandhi et al., 2021). Acid modification of kaolinite, moreover, enhances the number of acid centers on the surface, increases the specific surface area, and improves its catalytic efficacy. Kaolinite modified with hydrochloric acid can augment the acid activity of the clay's structure without compromising its basic integrity, thus exposing a greater number of active adsorption sites (Chen et al., 2018). hydrochloric acid-modified kaolinite nanosized zero-valent iron addresses some of the limitations associated with nZVI/H_2O_2, such as agglomeration and self-oxidation, making it a more efficient material for

treating MO wastewater (Elfadly et al., 2017; Rabie et al., 2018). Our investigation centered around the Fenton-like reaction induced by hydrochloric acid-modified kaolinite supported nanosized zero-valent iron (mk-nZVI). Our goal was to broaden the pH application range to effectively degrade MO-containing wastewater and to examine the factors influencing the efficiency of an mk-nZVI/H_2O_2 system for MO degradation. In addition, we delved into the reaction mechanism, an exploration that contributes to the development of processes intended to enhance aquatic environments.

2 Materials and Methods

2.1 Materials

Methyl orange ($C_{14}H_{14}N_3SO_3Na$) was purchased from Beijing Bellingwei Technology Co., Ltd. H_2O_2 (30%), sodium borohydride($NaBH_4$), ferric chloride hexahydrate ($FeCl_3{\cdot}6H_2O$), anhydrous ethanol, n-butanol and potassium iodide (KI) were all provided by Sinopharm Chemical Reagent Co., Ltd, China. All the aforementioned reagents were of analytical grade and were used without further purification. All solutions were prepared with deionized water, and nitrogen was blown into all prepared solutions for deoxidization.

2.2 Composite Preparation

2.2.1 Preparation of nZVI

The chemical reaction involved in liquid-phase reduction, which was adopted in this study, can be expressed as follows:

$$4Fe^{3+} + 3BH_4^- + 9H_2O \rightarrow 4Fe^0 + 3H_2BO_3^- + 12H^+ + 6H_2 \quad (1)$$

$FeCl_3{\cdot}6H_2O$ (4.83 g) was dissolved in a solution of anhydrous ethanol and deionized water (3:7; 50 mL) and subsequently transferred into a three-neck flask, one neck of which had a mechanical agitator attached. The solution was then stirred under a N_2 atmosphere for 30 min. $NaBH_4$ (3 g) was subsequently dissolved in 100 mL of deionized water, and the resulting solution was added dropwise to a three-neck flask using a peristaltic pump at a rate of one drop per second with intense stirring (500 rpm) to facilitate the reaction. The $NaBH_4$ solution was stirred for 30 min after it was completely added. Finally, a magnet was used to attract the particles in the bottom of the three-neck flask, the waste liquid was poured out, the leftover components were cleaned with anhydrous ethanol three times, then sealed for storage. All these steps were conducted under an N_2 atmosphere.

2.2.2 Preparation of Hydrochloric Acid-Modified Kaolinite Supported Nanosized Zero-Valent Iron (mk-nZVI)

Preparation of hydrochloric acid-modified kaolinite (mk): An HCl solution (100 mL, 25 wt%) was blended with 25 g of kaolinite, followed by a rigorous stirring process for 2 h, facilitated by a mechanical stirrer. After thorough agitation, the modified kaolinite was centrifuged and rinsed until a neutral pH was achieved. Subsequent processes involved filtration, drying at ambient temperature for a span of 36 h, and then grinding and sieving (100 mesh). The resulting mk was transferred to a glassdesiccator, sealed, and preserved for further analysis.

Preparation of mk-nZVI: The synthesis of mk-nZVI was accomplished by employing a method similar with the Sect. 2.2.1. The $FeCl_3{\cdot}6H_2O$ solution was poured into a three-necked flask and stirred for half an hour under a nitrogen atmosphere. Following this, 2.33 g of the mk was introduced, and the system was once again stirred under a nitrogen atmosphere for an additional 30 min. Subsequently, 3 g of $NaBH_4$ was dissolved in 100 mL of deionized water. The remainder of the procedure followed the steps outlined in Sect. 2.2.1.

2.3 Characterization

The concentration of MO in the aqueous solution was determined at 464 nm using UV–Vis spectrophotometry (Mapada, UV-6 series dual beam scanning, China). The morphology and elemental distribution of mk-nZVI were examined via Scanning Electron Microscopy (SEM) (ZEISS, SIGMA500, Germany). Structural and compositional analyses of the materials were conducted through X-ray diffraction scans ranging from 10° to 70°, utilizing an X-ray diffractometer (Bruker, D8-Advance, Germany) to characterize

the composite material. Fourier Transform Infrared Spectroscopy (FTIR) (Thermo Scientific, Nicolet-IS5, USA) was used to identify functional groups on the surface of composite material within the range of 500 to 4000 cm^{-1}. X-ray Photoelectron Spectroscopy (XPS) (Thermo Scientific, ESCALAB 250XI, USA) was employed to study the Fe species on the mk-nZVI surface. The binding energies of the spectra were corrected using the hydrocarbon component of adventitious carbon at 284.8 eV. XPS data fitting was performed using XPSPEAK 41.

2.4 Experimental Methods

A MO solution (100 mL) of a predetermined concentration was introduced into a 250-mL stoppered conical flask, maintaining its pH of 5.6. This flask was then situated within a temperature-controlled oscillating chamber. A defined quantity of mk-nZVI and H_2O_2 (74.8 mmol/L) were supplemented, instigating the reaction as the flask oscillated at a rate of 180 rotations per minute. The reaction was permitted to continue for a duration of 90 min, throughout which the MO concentration was intermittently assessed. Further examination was conducted on the influence of variables including composite dosage, reaction temperature, initial solution concentration, and H_2O_2 concentration on the decolorization of MO. All experiments were performed in duplicate, with data presented as mean ± standard deviation.

3 Results and Discussion

3.1 Characterization of Composites

FTIR spectra of the mk-nZVI composite and nZVI are shown in Fig. 1. The –OH and –COOH stretching vibration absorption peak appeared at 3429.68 cm^{-1} and 1625.86 cm^{-1}. The stretching vibration absorption peak of Si–O–Si, absorption peak of Si–OH, and bending vibration absorption peak of Si appeared at 1099.54, 895.15, and 465.78 cm^{-1}, respectively (Quintelas et al., 2011).

The XRD patterns are depicted in Fig. 2. nZVI exhibited a diffraction peak at 44.67°. There were no iron oxide peaks in the XRD pattern of nZVI (Petala et al., 2013), implying a predominance

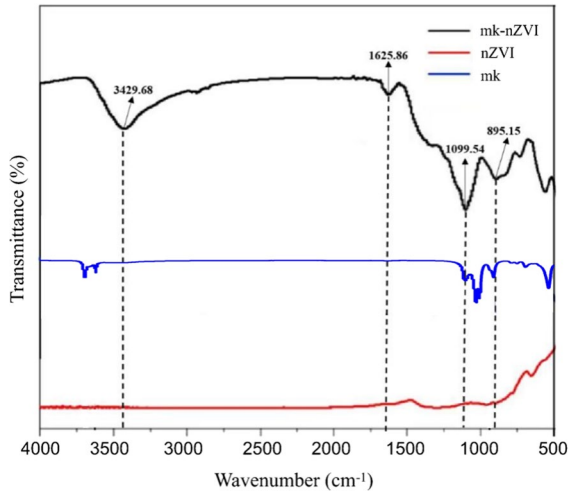

Fig. 1 FTIR spectra of mk, nZVI, and mk-nZVI

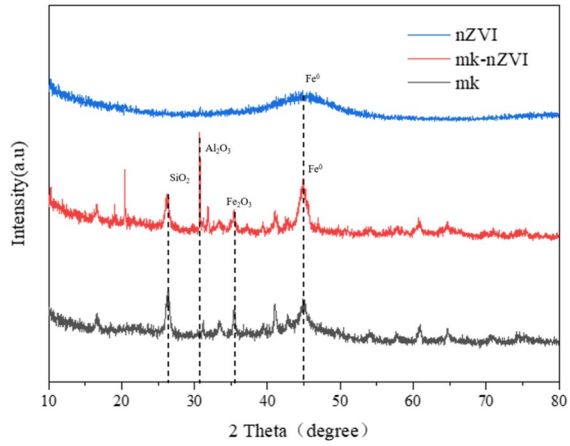

Fig. 2 XRD patterns of mk, nZVI, and mk-nZVI

of Fe^0. Comparison with the standard card of Fe (JCPDS No.06–0696) indicated that the material exhibited the plane diffraction of an α-Fe body-centered cubic structure (Zhou et al., 2021). The characteristic peak at $2\theta = 44.98°$ confirmed the existence of zero-valent iron in mk-nZVI, and the diffraction peak of the composite material was sharper and narrower than that without the composite material, indicating successful loading of Fe^0 nanoparticles (Fan et al., 2009). In addition, the peaks at 26.21° and 31° are characteristic peaks of kaolinite, reflecting the typical structure of kaolinite. The XPS results are depicted in

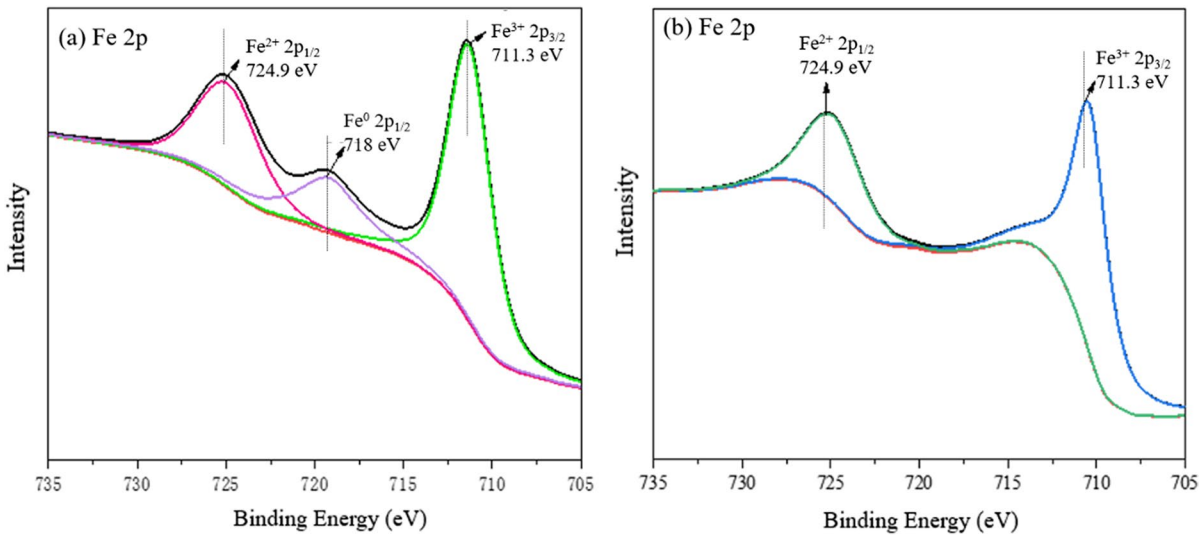

Fig. 3 (**a**) pre-reaction and (**b**) post-reaction XPS spectra of mk-nZVI

Fig. 3. Figure 3 (a) indicates the presence of different states of Fe in mk-nZVI, with the binding energies of 711.3 eV and 724.9 eV corresponding to Fe^{3+} $2p_{3/2}$ and Fe^{2+} $2p_{1/2}$, respectively; this confirms the presence of iron oxide in the mk-nZVI (Bagus et al., 2020), likely resulting from oxidation of the sample. Moreover, Fe^0 could be detected at 718 eV, suggestive of nZVI coating on the acid-modified kaolinite. Figure 3 (b) shows the XPS profiles obtained after the reaction, which indicate that the Fe peaks related to the 2p orbital slightly changed (724.8 eV and 710.37 eV), and the Fe^0 peak at 718 eV disappeared; moreover, the binding energies of Fe^{2+} $2p_{1/2}$ and Fe^{3+} $2p_{3/2}$ both increased slightly, indicating complete oxidation of Fe^0. The SEM images (Fig. 4) demonstrate that nZVI is uniformly coated onto the acid-modified kaolinite.

3.2 Degradation Experiments of MO

The results for degradation of MO under different reaction systems are shown in Fig. 5. Over the course of 90-min reaction, individual addition of mk and H_2O_2 achieved MO removal rates of 61.09% and 56.45%, respectively. Treatments with mk/H_2O_2, mk-nZVI, nZVI/H_2O_2, and the mk-nZVI/H_2O_2-based Fenton-like reaction resulted in MO removal rates of 72.55%, 80.32%, 86.19%, and 96.56%, respectively.

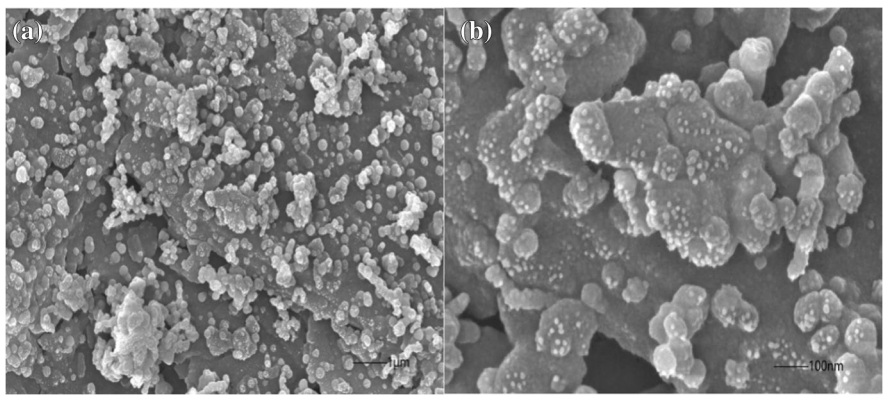

Fig. 4 SEM images of mk-nZVI (**a**) at a scale of 1 μm and (**b**) at a scale of 100 nm

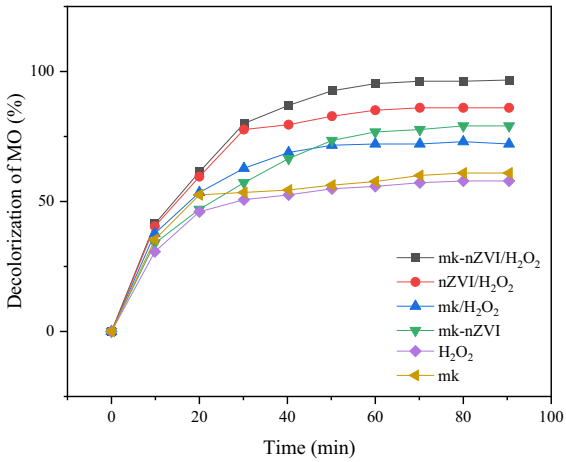

Fig. 5 Degradation of MO under different reaction systems. Experimental condition: T = 25 °C, MO concentration = 100 mg/L, pH = 5.6, 2 g/L mk; 20 mL of H_2O_2 (74.8 mmol/L); 2 g/L mk-nZVI; 2 g/L mk + 20 mL of H_2O_2 (74.8 mmol/L); 2 g/L nZVI + 20 mL of H_2O_2 (74.8 mmol/L), and 2 g/L mk-nZVI + 20 mL of H_2O_2 (74.8 mmol/L)

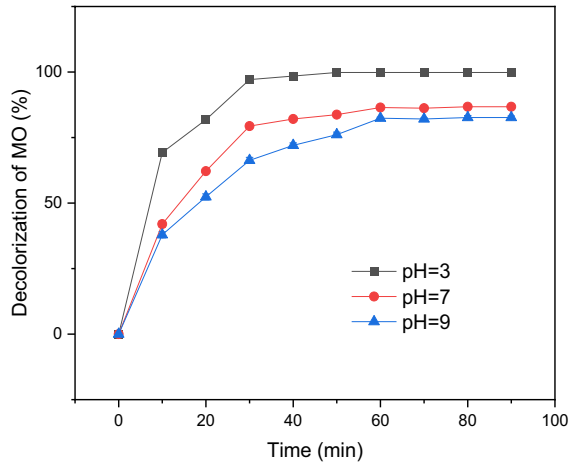

Fig. 6 Effect of pH on degradation of MO. Experimental condition: MO concentration = 100 mg/L, T = 25 °C, pH = 3, 7, and 9, mk-nZVI dose = 2 g/L, H_2O_2 concentration = 78.4 mmol/L

These results suggest that the mk-nZVI/H_2O_2-based Fenton-like reaction enhanced the degradation of MO. This improvement is presumably attributable to the synergistic effect of MO adsorption on kaolinite and the nZVI-catalyzed Fenton reaction, thereby increasing the efficiency of degradation. The reactions involved in the MO treatment via the mk-nZVI/H_2O_2-based Fenton-like reaction, as described by Lin et al. (2017), are outlined below. Initially, nZVI donates two electrons, which are transferred to H_2O_2, catalyzing its oxidation to Fe^{2+} as shown in Eq. (2). This is followed by the production of ·OH by the Fenton oxidation of Fe^{2+} and H_2O_2 as shown in Eq. (3). Furthermore, H_2O_2 undergoes decomposition as depicted in Eq. (5).

$$Fe^0 + 2H^+ \rightarrow Fe^{2+} + H_2 \quad (2)$$

$$Fe^{2+} + H_2O_2 \rightarrow Fe^{3+} + \cdot OH + OH^- \quad (3)$$

$$2Fe^{3+} + Fe^0 \rightarrow 3Fe^{2+} \quad (4)$$

$$2H_2O_2 \rightarrow 2H_2O + O_2 \quad (5)$$

3.2.1 *Effect of pH on Degradation of MO*

The data demonstrated that the degradation rate of MO increased as pH values decreased (Fig. 6). At a pH level of 3, the rate of MO degradation reached 99.84%, suggesting near-total degradation. However, at pH 7 and pH 9, the MO degradation rates were 86.74% and 82.65% respectively. This can be attributed to the fact that a pH of approximately 3–4, commonly used in traditional Fenton systems, effectively catalyzes H_2O_2 to produce ·OH radicals. In Fenton-like treatments, such as the mk-nZVI/H_2O_2 used in this study (where mk-nZVI acts as a Fenton-like catalyst), the generation of ·OH radicals primarily occurs on the surface of mk-nZVI particles. This process is less influenced by the pH of the solution, thereby expanding the pH range suitable for the reaction (Feng et al., 2006).

The degradation of MO using a traditional Fenton reaction was compared with that achieved by the mk-nZVI/H_2O_2-based Fenton-like reaction under similar conditions across a pH range of 5.6–9.0 (Fig. 7). With comparable pH values, the Fenton-like reaction proved more effective than the traditional Fenton process in degrading MO. When the initial solution pH was 5.6, MO degradation rates of 96.56% and 73.1% were achieved by the Fenton-like reaction and the traditional Fenton reaction,

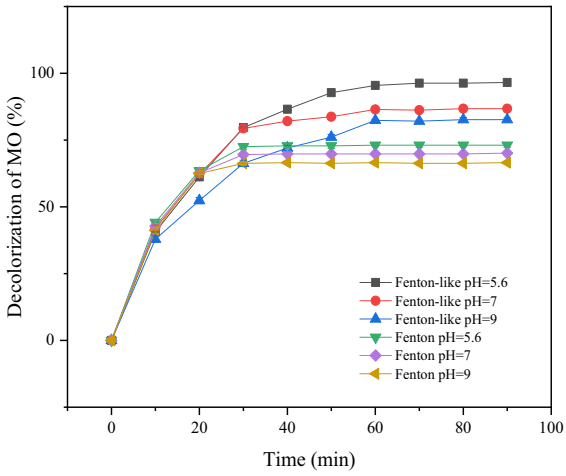

Fig. 7 Effect of the Fenton-like and traditional Fenton methods on degradation of MO

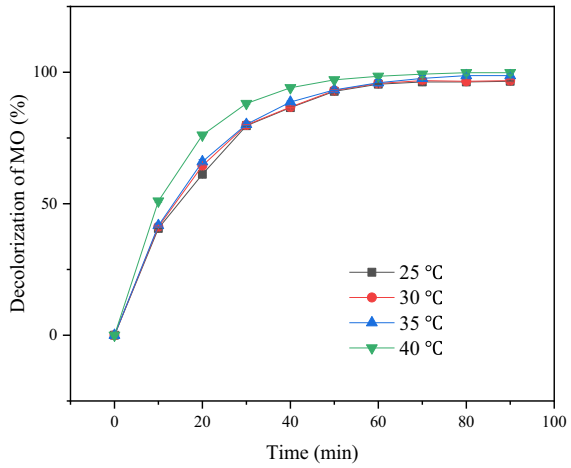

Fig. 8 Effect of reaction temperature on degradation of MO. Experimental condition: MO concentration = 100 mg/L, T = 25 °C, 30 °C, 35 °C and 40 °C, pH = 5.6, mk-nZVI dose = 2 g/L, H_2O_2 concentration = 78.4 mmol/L

respectively. Under acidic conditions, the functional groups on the surface of the composite material acquire a positive charge due to a protonation reaction. This enables the composite material's surface to attract anions electrostatically, facilitating the formation of hydrogen bonds with the azo groups in the solution, thereby aiding in the removal of MO (Gao et al., 2019; Vithanage et al., 2017).

3.2.2 *Effect of Reaction Temperature on Degradation of MO*

The results indicate that the degradation rate of MO escalates with a rise in temperature, escalating from 96.56% at 25 °C to 99.8% at 40 °C. This phenomenon is attributable to the fact that enhanced temperature instigates a vigorous thermal motion of MO molecules within the solution. This dynamic motion consequently augments the likelihood of interaction between these molecules and the active sites of mk-nZVI. Acting as the catalyst in the Fenton-like reaction, mk-nZVI propels H_2O_2 to generate a greater quantity of ·OH (Hassan et al., 2020), which in turn enhances the degradation rate of MO (Fig. 8).

3.2.3 *Effect of mk-nZVI Dose on Degradation of MO*

As Fig. 9 demonstrates, the degradation rate of MO correlates positively with the increasing concentration of mk-nZVI (Li et al., 2015). The systems incorporating 2 g/L and 3 g/L mk-nZVI achieved MO degradation rates of 96.56% and 98.2%, respectively. However, a marginal increase of only 1.64% was observed in the degradation rate when the dosage of mk-nZVI was elevated from 2 to 3 g/L. This finding suggests that a specific amount of mk-nZVI is adequate to catalyze the decomposition of MO given a certain concentration of H_2O_2.

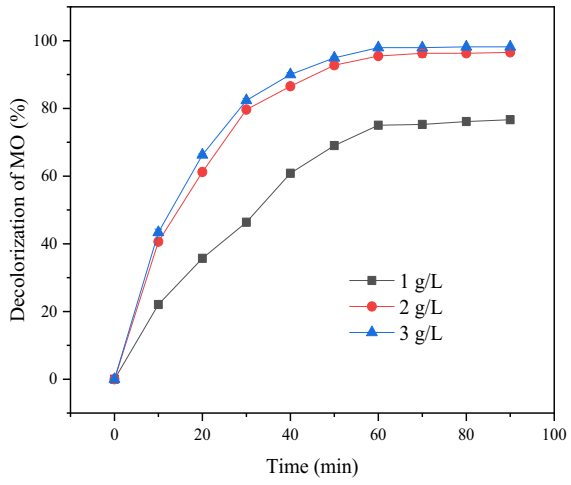

Fig. 9 Effect of mk-nZVI dose on degradation of MO. Experimental condition: MO concentration = 100 mg/L, T = 25 °C, pH = 5.6, mk-nZVI dose = 1, 2, and 3 g/L, H_2O_2 concentration = 78.4 mmol/L

Consequently, 2 g/L has been identified as the optimal dosage of mk-nZVI.

3.2.4 *Effect of MO Concentration on Degradation of MO*

Our investigation revealed a diminishing degradation rate of MO concurrent with an increase in the initial concentration of the solution. A maximum degradation rate of merely 54.54% was achieved at an initial MO concentration of 200 mg/L. This trend could be attributed to the elevated solution concentration resulting in the adsorption of an excess of MO molecules onto the surfaces of mk-nZVI, thereby reducing the number of active sites and subsequently suppressing the production of ·OH (Xue et al., 2009). Furthermore, a high concentration solution tends to generate an abundance of intermediates during the reaction, which consume a considerable amount of OH (Hamad et al., 2018) (Fig. 10).

3.2.5 *Effect of H_2O_2 Concentration on Degradation of MO*

The effect of H_2O_2 concentration on degradation of MO were scrutinized, as illustrated in Fig. 11. The findings revealed that an optimal MO degradation rate of 96.56% was attained at a H_2O_2 concentration

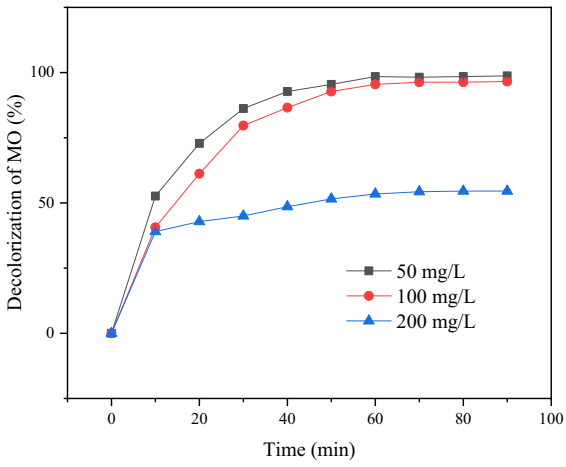

Fig. 10 Effect of MO concentration on degradation of MO. Experimental condition: MO concentration = 50, 100, and 200 mg/L, T = 25 °C, pH = 5.6, mk-nZVI dose = 2 g/L, H_2O_2 concentration = 78.4 mmol/L

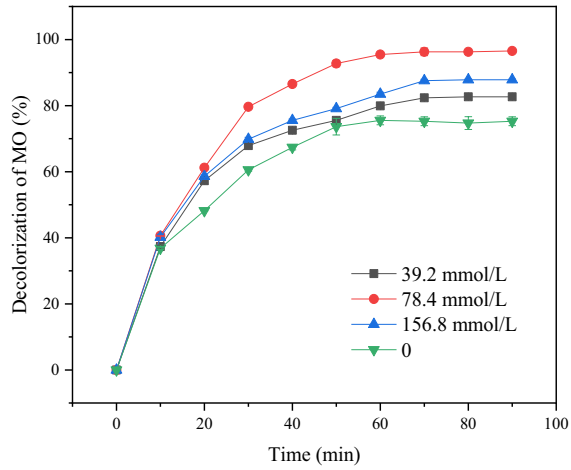

Fig. 11 Effect of H_2O_2 concentration on degradation of MO. Experimental condition: MO concentration = 100 mg/L, T = 25 °C, pH = 5.6, mk-nZVI dose = 2 g/L, H_2O_2 concentration = 0, 39.2, 78.4 and 156.8 mmol/L

of 78.4 mmol/L. This could be due to the propensity of excessive H_2O_2 to induce the quenching of ·OH. Furthermore, ·OH can undergo decomposition, thereby diminishing the degradation rate of MO, as demonstrated in Eqs. (6), (7), and (8).

$$nZVI + 2H_2O_2 \rightarrow Fe^{2+} + 2 \cdot OH + 2OH^- \quad (6)$$

$$H_2O_2 + \cdot OH \rightarrow H_2O + 2 \cdot OOH \quad (7)$$

$$2 \cdot OOH + 2 \cdot H \rightarrow 2H_2O + O_2 \quad (8)$$

3.3 Degradation Kinetics of MO

The degradation of MO by the mk-nZVI/H_2O_2-based Fenton-like reaction was simulated using pseudo-first-order and pseudo-second-order kinetics models. The pseudo first-order dynamics model is expressed as follows:

$$\ln\left(\frac{C_t}{C_0}\right) = -k_{obs1} \cdot t \quad (9)$$

where, C_0 (mg/L) is the initial MO concentration, C_t (mg/L) is the MO concentration at t min, and k_{obs1} (min^{-1}) is the first-order reaction rate constant, which can be obtained from the slope of the $\ln(C_t/C_0)$–t

plot. The pseudo-second-order dynamics model is expressed as follows:

$$\ln\left(\frac{1}{C_t}-\frac{1}{C_0}\right)=k_{obs2}\cdot t \quad (10)$$

where, k_{obs2} (L/mg·min) is the second-order reaction rate constant, which can be obtained from the slope of the $\ln(1/C_t-1/C_0)$–t plot.

As indicated in Table 1, the R^2 value of the pseudo-first-order kinetics model exceeds 0.9. This suggests that the degradation of MO achieved through the mk-nZVI/H_2O_2-based Fenton-like reaction under varying temperatures align more closely with pseudo-first-order kinetics. This observation is congruent with the established understanding that the pseudo-first-order dynamics model can precisely depict the dynamic processes of distinct nZVI particles and loaded nZVI particles (Li et al., 2016). Graphical representations of the pseudo-first-order dynamic model are portrayed in Fig. 12. The temperature reduction from 40 °C to 25 °C resulted in a decline in the observed rate constant (k_{obs1}) from 0.0740 to 0.0407 min^{-1}. This suggests that the degradation of MO via the mk-nZVI/H_2O_2-based Fenton-like reaction at differing temperatures is indeed an endothermic process (Daud et al. 2010.

The Arrhenius formula is expressed as follows (Shi et al., 2011):

$$\ln K=-\frac{E_a}{RT}+\ln A_0 \quad (11)$$

where, E_a (J/mol) is the apparent activation energy, A_0 (min^{-1}) is the pre-exponential factor, K (min^{-1}) is the pseudo-first-order adsorption rate constant, R (8.314 J/mol·K) is the gas constant, and T (K) is the reaction temperature. E_a was determined using the

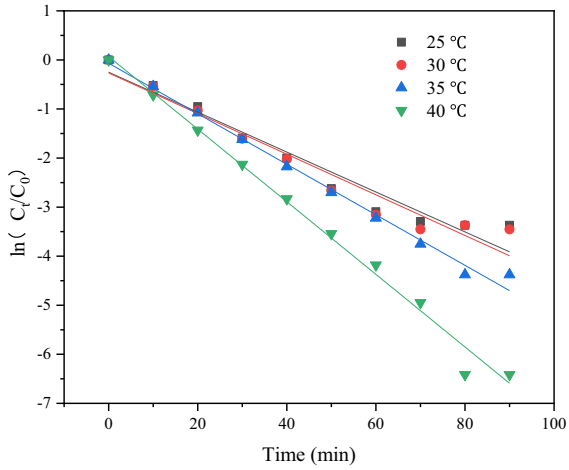

Fig. 12 Pseudo first-order kinetic model fitting under different temperature conditions

pseudo-first-order reaction rate constant, k_{obs1}, and the slope of the line was obtained by plotting ln K against 1/T. E_a was estimated to be 31.05 kJ/mol, indicating that the degradation of MO by the mk-nZVI/H_2O_2-based Fenton-like process at different temperatures was a chemically controlled surface-restricted reaction that exhibited a large activation energy (> 29 kJ/mol) (Jin et al., 2016).

3.4 Degradation Isotherm of MO

MO solutions, with distinctive initial concentrations (50, 100, and 200 mg/L), were formulated at a temperature of 25 °C. A dosage of 2 g/L mk-nZVI and a reaction duration of 90 min were employed. The acquired experimental data were simulated using both Langmuir and Freundlich isotherm models, aiming to deduce the isotherm

Table 1 Kinetic parameters of degradation of MO

Temperature /°C	C_0/(mg·L^{-1})	Pseudo-first-order model		Pseudo-second-order model	
		k_{obs1}/min^{-1}	r^2	k_{obs2} /[L·(mg·min)$^{-1}$]	r^2
40	100	0.0740	0.9906	0.0691	0.9177
35	100	0.0515	0.9925	0.0479	0.8439
30	100	0.0414	0.9463	0.0377	0.7622
25	100	0.0407	0.9479	0.0371	0.7515

type that could most accurately depict the degradation mechanism.

The Langmuir isotherm model is expressed as follows:

$$q_e = \frac{Kq_mC_e}{1 + KC_e} \quad (12)$$

where, q_e ($mg \cdot g^{-1}$) is the adsorption capacity, q_m ($mg \cdot g^{-1}$) is the maximum adsorption capacity, K (L/mg) is the Langmuir constant, and C_e (mg/L) is the equilibrium solute concentration.

The Freundlich adsorption isotherm model is expressed as follows:

$$q_e = KC_e^{1/n} \quad (13)$$

where, K and n are Freundlich constants. The simulation results of the two adsorption isotherm models are shown in Table 2. Table 2 highlights that the R^2 value deduced from the Langmuir model surpasses that of the Freundlich model. This suggests that the adsorption of MO onto mk-nZVI aligns more closely with the Langmuir model. It can be inferred that MO is uniformly adsorbed onto the surfaces of mk-nZVI, predominantly via monolayer adsorption.

3.5 Degradation Thermodynamic of MO

The degradation of MO by the mk-nZVI/H_2O_2-based Fenton-like reaction was evaluated at various temperatures. Accordingly, thermodynamic parameters, such as Gibbs free energy (ΔG^0), entropy (ΔS^0), and enthalpy (ΔH^0), were ascertained using the following equations (Pelalak et al., 2021):

$$\Delta G^0 = -RT\ln K_c, K_c = \frac{q_e}{C_e} \quad (14)$$

$$\ln K_c = \frac{\Delta S^0}{R} - \frac{\Delta H^0}{RT} \quad (15)$$

where, K (mL/g) is the equilibrium constant. The values of ΔG^0, ΔS^0, and ΔH^0 were determined using ln K_c and 1/T (Table 3). Table 3 reveals that ΔH^0 is greater than zero, which designates the degradation of MO as an endothermic process. This, in turn, implies that the adsorption capacity intensifies with a rising temperature. Conventionally, when a reaction absorbs heat ranging from 80 to 200 $kJ \cdot mol^{-1}$, it is indicative of a chemical reaction. The energy required for physical adsorption tends to be relatively low, generally lying within the 0 to 20 $kJ \cdot mol^{-1}$ range, a finding consistent with the conclusions drawn in Sect. 3.3. A negative ΔG^0 signifies the spontaneous nature of the MO degradation process facilitated by the mk-nZVI/H_2O_2-based Fenton-like reaction. The growing absolute value of ΔG^0 with increasing temperature suggests that elevated temperatures could enhance the degradation of MO. The ΔS^0 being greater than zero implies that the observed degradation of MO represent a transition from an ordered to a disordered state.

3.6 Mechanism of Degradation of MO by mk-nZVI

Ultraviolet–visible (UV–vis) full-wavelength scanning was performed for varying durations of degradation, as depicted in Fig. 13. Characteristic absorption peaks appeared in the visible region at approximately 464 nm, which correspond to the behavior of the azo groups in MO. Additional absorption peaks were

Table 2 Isothermal parameters in the degradation of MO

Adsorbent	Langmuir model			Freundlich model		
mk-nZVI	$q_m/(mg \cdot g^{-1})$	K/ $(L \cdot mg^{-1})$	r^2	K $(mg \cdot g^{-1})$	1/n	r^2
	82.29	7.963	0.9915	66.26	0.220	0.8692

Table 3 Thermodynamic parameters of degradation of MO

Temperature/°C	ln K_c	$\Delta G^0/(kJ \cdot mol^{-1})$	$\Delta S^0/(kJ \cdot mol^{-1})$	$\Delta H^0/(kJ \cdot mol^{-1})$
40	8.716	21.967	573.841	157.006
35	6.668	16.806	564.949	
30	5.723	14.425	565.496	
25	5.638	13.975	573.475	

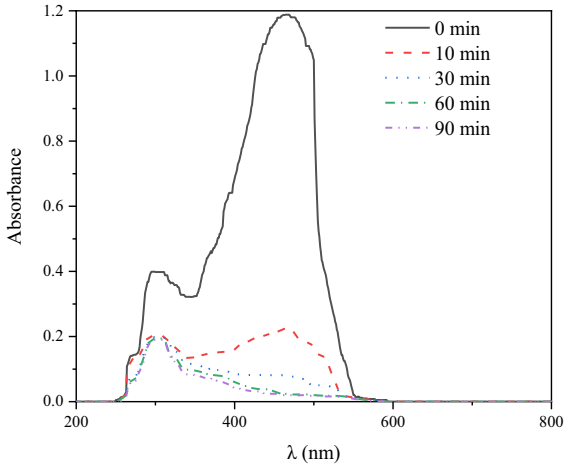

Fig. 13 UV–vis spectra of MO during degradation. Experimental condition: pH = 5.6, T = 25 °C, initial MO concentration = 100 mg/L, mk-nZVI dose = 2 g/L, H_2O_2 concentration = 78.4 mmol/L

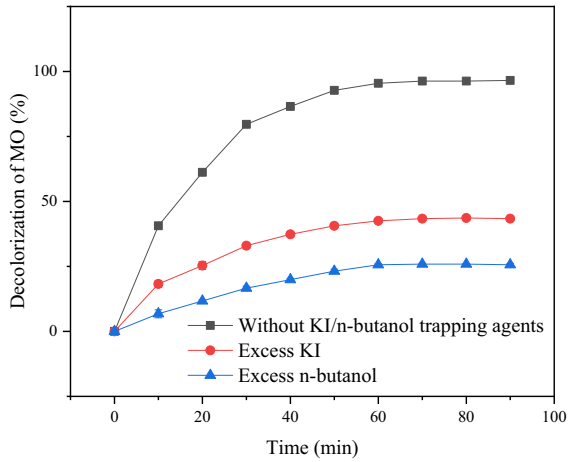

Fig. 14 Effects of excess KI and n-butanol on degradation of MO. Experimental condition: T = 25 °C, MO concentration = 100 mg/L, mk-nZVI dose = 2 g/L, H_2O_2 concentration = 78.4 mmol/L, pH = 5.6, excess n-butanol and KI were introduced into the reaction system

discernible in the 250–300 nm range, potentially corresponding to aromatic compounds (El-Desoky et al., 2010). The characteristic azo group peak at 464 nm gradually diminished and vanished with prolonged reaction time, signifying that the mk-nZVI/H_2O_2-based Fenton-like reaction could effectively cleave the azo bonds in MO molecules. Furthermore, the characteristic peak of the aromatic compounds gradually lessened, affirming the system's ability to effectively degrade MO.

KI and n-butanol were employed as ·OH scavengers to ascertain the potential role of ·OH as the primary radical in MO degradation catalyzed by mk-nZVI. n-butanol can capture ·OH both at the reaction interface and in solution, whereas KI can trap ·OH solely at the reaction interface (Xu & Wang, 2011). The results demonstrated that an MO degradation rate of 96.56% was achieved in the absence of n-butanol (Fig. 14). However, the degradation rate diminished from 96.56 to 40.09% upon introducing excess n-butanol, suggesting that MO is primarily decomposed by the attack of ·OH radicals (encompassing both surface-bounded and free ·OH). With the addition of excess KI, which scavenges ·OH produced at the mk-nZVI surface, the degradation rate decreased from 96.56 to 43.36%. This result signifies that surface-bounded ·OH plays a substantial role in the degradation of MO.

Expanding on the preceding discussion, Fig. 15 illustrates the process through which the mk-nZVI/H_2O_2-based Fenton-like reaction degrades MO. ·OH are predominantly generated via two pathways. One pathway involves the Fenton-like reaction on the particle surface between adsorbed H_2O_2 molecules and mk-nZVI, resulting in surface-bound hydroxyl radicals ($\cdot OH_a$). The second pathway entails the Fenton reaction between H_2O_2 molecules and Fe leached from the mk-nZVI surface, yielding free hydroxyl radicals ($\cdot OH_b$). It is important to underscore that MO and H_2O_2 molecules initially adsorb onto the mk-nZVI surface, thus fostering the reaction between the oxidant and the active site. This interaction generates free radicals within the solid phase. According to Eq. (3), Fe^{2+} reacts with H_2O_2 in both pathways, and is subsequently oxidized to Fe^{3+}. As expressed in Eqs. (16) and (17), the regeneration of Fe^{2+} is facilitated by reducing Fe^{3+} with H_2O_2, which then leads to the formation of less reactive species such as $HO_2\cdot$ and $O_2\cdot$ (Barndok et al., 2016). As depicted in Eqs. (18) through (21), the formed $O_2\cdot$ reacts with H_2O molecules to generate additional ·OH radicals while concurrently producing and consuming H_2O_2. A compound of $HO_2\cdot$ radicals in the liquid or solid phase can further yield H_2O_2, H_2O, or O_2 molecules, as illustrated in Eqs. (23) and (24) (Taha & Ibrahim, 2014). Finally, the Eq. (25) reveals that MO react with both

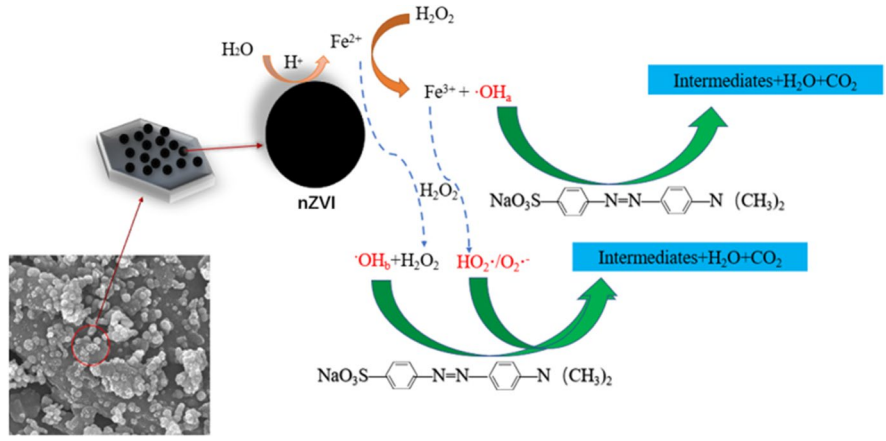

Fig. 15 Mechanism of degradation of MO by mk-Nzvi

free radicals, $\cdot OH_a$ and $\cdot OH_b$, alongside $HO_2\cdot$ and $O_2\cdot$, to form intermediates, carbon dioxide, and water.

$$Fe^{3+} + H_2O_2 \rightarrow Fe^{2+} + HO_2^{\cdot}/O_2^{\cdot -} + H^+ \quad (16)$$

$$Fe^{3+} + HO_2^{\cdot} \rightarrow Fe^{2+} + O_2 + H^+ \quad (17)$$

$$O_2^{\cdot -} + O_2^{\cdot -} + 2H^+ \rightarrow H_2O_2 + O_2 \quad (18)$$

$$O_2^{\cdot -} + 2H^+ \rightarrow HO_2^{\cdot} \quad (19)$$

$$O_2^{\cdot -} + H_2O \rightarrow \cdot OH_a + OH^- \quad (20)$$

$$O_2^{\cdot -} + H_2O \rightarrow HO_2^{\cdot} + HO^- \quad (21)$$

$$O_2^{\cdot -} + H_2O_2 \rightarrow O_2 + HO^- + \cdot OH_a \quad (22)$$

$$HO_2^{\cdot} + HO^{\cdot} \rightarrow H_2O + O_2 \quad (23)$$

$$HO_2^{\cdot} + HO_2^{\cdot} \rightarrow H_2O_2 + O_2 \quad (24)$$

$$\cdot OH_a / \cdot OH_b / HO_2^{\cdot} / O_2^{\cdot -} + MO \rightarrow Intermediates + CO_2 + H_2O \quad (25)$$

In conducting a comparative analysis, the maximum removal capacity (q_m) of this study is juxtaposed with the experimental parameters for removal of MO by various removal materials reported in extant literature, as summarized in Table 4. The results reveal that mk-nZVI exhibits a superior removal capacity (82.29 mg/g) and a heightened proficiency in degradation MO from aqueous solution. Nevertheless, the evaluation of removal materials viability is contingent upon factors such as efficiency, availability, cost-effectiveness, and ease of preparation. Consequently, this study proposes

Table 4 Comparing the removal performance of mk-nZVI and other materials for MO

MO removal materials	C_0(mg/L^{-1})	Initial pH	T(℃)	Volume of MO (mL)	q_m(mg/g)	References
Sugar scum powder	100	7.2	22	50	15.24	(EI Maguana et al., 2020)
γ- Fe_2O_3/chitosan composite films	10–60	NA	37	50	29.41	(Jiang et al., 2012)
γ- Fe_2O_3 crosslinked chitosan composite	30	6.6	27	50	29.46	(Zhu et al., 2010b)
γ- Fe_2O_3/chitosan/kaolin composite	20	2.9–11.4	37	50	34.29	(Zhu et al., 2010a)
AlgN-CTAB	0–300	5	27	25	76.48	(Buhani et al., 2021)
Zeolite NaA/CuO	50	7	25	100	79.49	(Mekatel et al., 2015)
Crosslinked chitosan beads	20	3	25	50	79.55	(Sabarudin & Madjid, 2021)
Goethite/chitosan beads	100	3	65	30	84	(Munagapati et al., 2017)
mk-nZVI/H_2O_2	100	5.6	25	100	82.29	This study

that the mk-nZVI, with its exceptional degradability, serves as a promising material capable of effectively removing MO from water environments.

4 Conclusion

This investigation found that using the mk-nZVI under specified conditions—initial MO solution concentration of 100 mg/L, reaction temperature of 25 °C, mk-nZVI dose of 2 g/L, and H_2O_2 concentration of 74.8 mmol/L—an MO degradation rate of 96.56% was attained. The mk-nZVI/H_2O_2-based Fenton-like reaction demonstrated superior efficacy compared to the traditional Fenton system within a pH range of 5.6–9.0. UV–Vis spectra of MO subjected to degradation by the mk-nZVI/H_2O_2-based Fenton-like reaction indicated that the mk-nZVI composite could effectively dismantle the azo structure of MO. Mechanistic elucidation of the H_2O_2-induced degradation of MO by the mk-nZVI composite revealed that surface-bounded ·OH plays a substantial role in the degradation of MO. Given its simplicity, environmental friendliness, cost-effectiveness, and efficiency in treating methyl orange-contaminated wastewater, the synthesized hydrochloric acid-modified kaolinite supported nanosized zero-valent iron represents a promising material for future applications.

Acknowledgements This work was supported by Natural Science Foundation of Chongqing, China (cstc2021jcyj-bshX0231, cstc2020jcyj-msxmX0763, cstc2021jcyj-msxmX0328).

Data Availability The data presented in this study are included in the article.

References

Arts, A., Schmuhl, R., de Groot, M. T., & van der Schaaf, J. (2021). Fast initial oxidation of formic acid by the Fenton reaction under industrial conditions. *Journal of Water Process Engineering, 40*, 101780.

Bagus, P. S., Nelin, C. J., Brundle, C. R., Crist, B. V., Lahiri, N., & Rosso, K. M. (2020). Covalency in Fe_2O_3 and FeO: Consequences for XPS satellite intensity. *The Journal of Chemical Physics, 153*(19), 4702.

Barndok, H., Blanco, L., Hermosilla, D., & Blanco, A. (2016). Heterogeneous photo-Fenton processes using zero valent iron microspheres for the treatment of wastewaters contaminated with 1,4-dioxane. *Chemical Engineering Journal, 284*, 112–121.

Bastidas, G. K. G., Sierra, C. A., & Ramirez, H. R. Z. (2018). Heterogeneous Fenton oxidation of Orange II using iron nanoparticles supported on natural and functionalized fique fiber. *Journal of Environmental Chemical Engineering, 6*(4), 4178–4188.

Buhani, S., Miftahza, N., Permatasari, D., & Sumadi. (2021). Improved Adsorption Capacity of Nannochloropsis sp. through Modification with Cetyltrimethylammonium Bromide on the Removal of Methyl Orange in Solution. *Adsorption Science & Technology, 2021*, 1–14.

Chen, H., Cheng, H., Zhou, F., Chen, K., Qiao, K., Lu, X., Ouyang, P., & Fu, J. (2018). Catalytic fast pyrolysis of rice straw to aromatic compounds over hierarchical HZSM-5 produced by alkali treatment and metal-modification. *Journal of Analytical and Applied Pyrolysis, 131*, 76–84.

Daud, N. K., & Hameed, B. H. (2010). Fenton-like oxidation of reactive black 5 solution using iron–Montmorillonite K10 catalyst. *Journal of Hazardous Materials, 176*(1), 1118–1121.

De Gisi, S., Lofrano, G., Grassi, M., & Notarnicola, M. (2016). Characteristics and adsorption capacities of low-cost sorbents for wastewater treatment: A review. *Sustainable Materials and Technologies, 9*, 10–40.

El-Desoky, H. S., Ghoneim, M. M., & Zidan, N. M. (2010). Decolorization and degradation of Ponceau S azo-dye in aqueous solutions by the electrochemical advanced Fenton oxidation. *Desalination, 264*(1), 143–150.

Elfadly, A. M., Zeid, I. F., Yehia, F. Z., Abouelela, M. M., & Rabie, A. M. (2017). Production of aromatic hydrocarbons from catalytic pyrolysis of lignin over acid-activated bentonite clay. *Fuel Processing Technology, 163*, 1–7.

El Maguana, Y., Elhadiri, N., Benchanaa, M., & Chikri, R. (2020). Adsorption Thermodynamic and Kinetic Studies of Methyl Orange onto Sugar Scum Powder as a Low-Cost Inorganic Adsorbent. *Journal of Chemistry, 2020*, 9165874.

Fan, J., Guo, Y., Wang, J., & Fan, M. (2009). Rapid decolorization of azo dye methyl orange in aqueous solution by nanoscale zerovalent iron particles. *Journal of Hazardous Materials, 166*, 904–910.

Feng, J., Hu, X., & Yue, P. L. (2006). Effect of initial solution pH on the degradation of Orange II using clay-based Fe nanocomposites as heterogeneous photo-Fenton catalyst. *Water Research, 40*(4), 641–646.

Galdames, A., Ruiz-Rubio, L., Orueta, M., Sánchez-Arzalluz, M., & Vilas-Vilela, J. L. (2020). Zero-valent iron nanoparticles for soil and groundwater remediation. *International Journal of Environmental Research and Public Health, 17*(16), 5817.

Gandhi, D., Bandyopadhyay, R., & Soni, B. (2021). Zeolite Y from kaolin clay of Kachchh, India: Synthesis, characterization and catalytic application. *Journal of the Indian Chemical Society, 98*(12), 100246.

Gao, X., Li, M., Zhao, Y., & Zhang, Y. (2019). Mechanistic study of selective adsorption of Hg^{2+} ion by porous alginate beads. *Chemical Engineering Journal, 378*, 122096.

Hamad, H., Bassyouni, D., El-Ashtoukhy, E. S., Amin, N., & Abd El-Latif, M. (2018). Electrocatalytic degradation and

minimization of specific energy consumption of synthetic azo dye from wastewater by anodic oxidation process with an emphasis on enhancing economic efficiency and reaction mechanism. *Ecotoxicology and Environmental Safety, 148*, 501–512.

Hassan, A. K., Al-Kindi, G. Y., & Ghanim, D. (2020). Green synthesis of bentonite-supported iron nanoparticles as a heterogeneous Fenton-like catalyst: Kinetics of decolorization of reactive blue 238 dye. *Water Science and Engineering, 13*(4), 286–298.

Jiang, R., Fu, Y. Q., Zhu, H. Y., Yao, J., & Xiao, L. (2012). Removal of methyl orange from aqueous solutions by magnetic maghemite/chitosan nanocomposite films: Adsorption kinetics and equilibrium. *Journal of Applied Polymer Science, 125*(S2), E540–E549.

Jin, X., Zhuang, Z., Yu, B., Chen, Z., & Chen, Z. (2016). Functional chitosan-stabilized nanoscale zero-valent iron used to remove acid fuchsine with the assistance of ultrasound. *Carbohydrate Polymers, 136*, 1085–1090.

Kapoor, R. T., Danish, M., Singh, R. S., Rafatullah, M., & Abdul Khalil, H. P. S. (2021). Exploiting microbial biomass in treating azo dyes contaminated wastewater: Mechanism of degradation and factors affecting microbial efficiency. *Journal of Water Process Engineering, 43*, 102255.

Li, D., Mao, Z., Zhong, Y., Huang, W. L., Wu, Y. D., & Peng, P. A. (2016). Reductive transformation of tetrabromobisphenol A by sulfidated nano zerovalent iron. *Water Research, 103*, 1–9.

Lin, J., Sun, M., Liu, X., & Chen, Z. (2017). Functional kaolin supported nanoscale zero-valent iron as a Fenton-like catalyst for the degradation of Direct Black G. *Chemosphere, 184*, 664–672.

Li, Q., Chen, Z. S., Wang, H. H., Yang, H., Wen, T., Wang, S. Q., Hu, B. W., & Wang, X. K. (2021). Removal of organic compounds by nanoscale zero-valent iron and its composites. *Science of the Total Environment, 792*, 148546.

Li, R., Jin, X., Megharaj, M., Naidu, R., & Chen, Z. (2015). Heterogeneous Fenton oxidation of 2,4-dichlorophenol using iron-based nanoparticles and persulfate system. *Chemical Engineering Journal, 264*, 587–594.

Marcon, L., Oliveras, J., & Puntes, V. F. (2021). In situ nanoremediation of soils and groundwaters from the nanoparticle's standpoint: A review. *Science of the Total Environment, 791*, 148324.

Mekatel, E. H., Amokrane, S., Aid, A., Nibou, D., & Trari, M. (2015). Adsorption of methyl orange on nanoparticles of a synthetic zeolite naa/cuo. *Comptes Rendus Chimie, 18*(3), 336–344.

Munagapati, V. S., Yarramuthi, V., & Kim, D. (2017). Methyl orange removal from aqueous solution using goethite, chitosan beads and goethite impregnated with chitosan beads. *Journal of Molecular Liquids, 240*, 329–339.

Park, M. H., Jeong, S., Lee, G., Park, H., & Kim, J. Y. (2019). Removal of aqueous-phase Pb(II), Cd(II), As(III), and As(V) by nanoscale zero-valent iron supported on exhausted coffee grounds. *Waste Management, 92*, 49–58.

Petala, E., Dimos, K., Douvalis, A., Bakas, T., Tucek, J., Zboril, R., & Karakassides, M. A. (2013). Nanoscale zero-valent iron supported on mesoporous silica: Characterization and reactivity for Cr(VI) removal from aqueous solution. *Journal of Hazardous Materials, 261*, 295–306.

Pelalak, R., Heidari, Z., Khatami, S. M., Kurniawan, T. A., Marjani, A., & Shirazian, S. (2021). Oak wood ash/GO/Fe3O4 adsorption efficiencies for cadmium and lead removal from aqueous solution: Kinetics, equilibrium and thermodynamic evaluation. *Arabian Journal of Chemistry, 14*(3), 102991.

Quintelas, C., Figueiredo, H., & Tavares, T. (2011). The effect of clay treatment on remediation of diethylketone contaminated wastewater: Uptake, equilibrium and kinetic studies. *Journal of Hazardous Materials, 186*(2), 1241–1248.

Rabie, A. M., Mohammed, E. A., & Negm, N. A. (2018). Feasibility of modified bentonite as acidic heterogeneous catalyst in low temperature catalytic cracking process of biofuel production from nonedible vegetable oils. *Journal of Molecular Liquids, 254*, 260–266.

Refat, M. S., Saad, H. A., Gobouri, A. A., Alsawat, M., Adam, A. M. A., & El-Megharbel, S. M. (2021). Charge transfer complexation between some transition metal ions with azo Schiff base donor as a smart precursor for synthesis of nano oxides: An adsorption efficiency for treatment of Congo red dye in wastewater. *Journal of Molecular Liquids, 345*, 117140.

Sabarudin, A., Madjid, A. D. R. (2021). Preparation and kinetic studies of cross-linked chitosan beads using dual crosslinkers of tripolyphosphate and epichlorohydrin for adsorption of methyl orange. *The Scientific World Journal*, 2021, 6648457.

Shi, B., Gao, S., Yu, H., Zhang, L., Song, C., & Huang, K. (2020). Fe^0 nanoparticles encapsulated in hollow porous nanosphere frameworks for efficient degradation of methyl orange. *Reactive and Functional Polymers, 153*, 104614.

Shi, L.-n, Zhang, X., & Chen, Z.-l. (2011). Removal of Chromium (VI) from wastewater using bentonite-supported nanoscale zero-valent iron. *Water Research, 45*(2), 886–892.

Tang, X., Li, Z., Liu, K., Luo, X., He, D., Ao, M., & Peng, Q. (2020). Sulfidation modified Fe_3O_4 nanoparticles as an efficient Fenton-like catalyst for azo dyes degradation at wide pH range. *Powder Technology, 376*, 42–51.

Tanwar, R., Kumar, S., & Mandal, U. K. (2017). Photocatalytic activity of PANI/Fe^0 doped BiOCl under visible light-degradation of Congo red dye. *Journal of Photochemistry and Photobiology a: Chemistry, 333*, 105–116.

Taha, M. R., & Ibrahim, A. H. (2014). Characterization of nano zero-valent iron (nZVI) and its application in sono-Fenton process to remove COD in palm oil mill effluent. *Journal of Environmental Chemical Engineering, 2*(1), 1–8.

Varjani, S., Rakholiya, P., Ng, H. Y., You, S. M., & Teixeira, J. A. (2020). Microbial degradation of dyes: An overview. *Bioresource Technology, 314*, 123728.

Vithanage, M., Herath, I., Joseph, S., Bundschuh, J., Bolan, N., Ok, Y. S., Kirkham, M. B., & Rinklebe, J. (2017). Interaction of arsenic with biochar in soil and water: A critical review. *Carbon, 113*, 219–230.

Waheed, A., Baig, N., Ullah, N., & Falath, W. (2021). Removal of hazardous dyes, toxic metal ions and organic pollutants from wastewater by using porous hyper-cross-linked polymeric materials: A review of recent advances. *Journal of Environmental Management, 287*, 112360.

Wang, Y., Jiang, L., Shang, H., Li, Q., & Zhou, W. (2020). Treatment of azo dye wastewater by the self-flocculating marine bacterium Aliiglaciecola lipolytica. *Environmental Technology & Innovation, 19*, 100810.

Xie, Z., Zhou, J., Wang, J., François-Xavier, C. P., & Wintgens, T. (2019). Novel Fenton-like catalyst γ-Cu-Al_2O_3-$Bi_{12}O_{15}C_{l6}$ with electron-poor Cu centre and electron-rich Bi centre for enhancement of phenolic compounds degradation and H_2O_2 utilization: The synergistic effects of σ-Cu-ligand, dual-reaction centres and oxygen vacancies. *Applied Catalysis B: Environmental, 253*, 28–40.

Xu, L., & Wang, J. (2011). A heterogeneous Fenton-like system with nanoparticulate zero-valent iron for removal of 4-chloro-3-methyl phenol. *Journal of Hazardous Materials, 186*(1), 256–264.

Xue, X., Hanna, K., Abdelmoula, M., & Deng, N. (2009). Adsorption and oxidation of PCP on the surface of magnetite: Kinetic experiments and spectroscopic investigations. *Applied Catalysis B: Environmental, 89*(3), 432–440.

Yu, R.-F., Chen, H.-W., Cheng, W.-P., Lin, Y.-J., & Huang, C.-L. (2014). Monitoring of ORP, pH and DO in heterogeneous Fenton oxidation using nZVI as a catalyst for the treatment of azo-dye textile wastewater. *Journal of the Taiwan Institute of Chemical Engineers, 45*(3), 947–954.

Zheng, J., Tang, X., Zhang, S., Huang, T., Zheng, H., & Sun, B. (2020). Relationship between the structure of chitosan-based flocculants and their performances in the treatment of model azo dyeing wastewater. *Chemosphere, 247*, 125920.

Zhou, Y. Y., Ma, L. Y., Li, R., Chen, D., Lu, Y. Y., Cheng, Y. Y., Lou, X. X., Xie, H., & Zhou, W. C. (2021). Enhanced heat-resistance property of aluminum-coated carbonyl iron particles as microwave absorption materials. *Journal of Magnetism and Magnetic Materials, 524*, 167681.

Zhu, H., Jiang, R., & Xiao, L. (2010a). Adsorption of an anionic azo dye by chitosan/kaolin/γ-Fe_2O_3 composites. *Applied Clay Science, 48*(3), 522–526.

Zhu, H., Jiang, R., Xiao, L., & Li, W. (2010b). A novel magnetically separable γ-Fe_2O_3/crosslinked chitosan adsorbent: Preparation, characterization and adsorption application for removal of hazardous azo dye. *Journal of Hazardous Materials, 179*, 251–257.